

# Single-Crystal Growth and Magnetic, Electronic Properties of the FCC Antiferromagnet $\text{Ba}_2\text{CoMoO}_6$

A.R.N. Hanna<sup>1,\*</sup>, M. M. Ferreira-Carvalho<sup>2,3</sup>, S.H. Chen<sup>2</sup>, C. F. Chang<sup>2</sup>, C. Y. Kuo<sup>4,5</sup>,

A.T.M.N. Islam<sup>1</sup>, R. Feyerherm<sup>1</sup>, L.H. Tjeng<sup>2</sup>, B. Lake<sup>1,6,\*</sup>

<sup>1</sup>Helmholtz-Zentrum Berlin für Materialien und Energie GmbH, 14109 Berlin, Germany

<sup>2</sup>Max Planck Institute for Chemical Physics of Solids, Nöthnitzer Str. 40, 01187 Dresden

<sup>3</sup>Germany and Institute of Physics II, University of Cologne, Zùlpicher Straße 77, 50937 Cologne, Germany

<sup>4</sup>Department of Electrophysics, National Yang Ming Chiao Tung University, Hsinchu, Taiwan

<sup>5</sup>National Synchrotron Radiation Research Center, Hsinchu, Taiwan

<sup>6</sup>Institut für Festkörperphysik, Technische Universität Berlin, Germany

\*Corresponding authors : [Abanoub.Hanna@helmholtz-berlin.de](mailto:Abanoub.Hanna@helmholtz-berlin.de), [Bella.lake@helmholtz-berlin.de](mailto:Bella.lake@helmholtz-berlin.de)

## Abstract

This work presents a comprehensive investigation of the structural, magnetic, and electronic properties of the double perovskite  $\text{Ba}_2\text{CoMoO}_6$  (BCMO). Single crystals were grown via floating zone and Czochralski growth techniques and characterized using a set of complementary methods. X-ray diffraction analysis confirmed that BCMO crystallizes in a face-centered cubic structure with space group  $Fm-3m$ . Magnetic susceptibility measurements exhibit antiferromagnetic ordering below  $T_N = 20.1(1)$  K, a spin-flop transition is observed at 26.5 kOe. Heat capacity measurements and entropy analysis are consistent with a  $J_{\text{eff}} = 1/2$  effective ground state for  $\text{Co}^{2+}$  ions. X-ray absorption spectroscopy provided insight into the local electronic structure, revealing the spin-orbit and crystal field splitting effects. The cluster-model analysis yields a g factor of 4.52, consistent with a spin-orbit-entangled ground state. Surface photovoltage spectroscopy revealed the strong optical response of this material. These findings enhance the understanding of FCC lattice antiferromagnets and suggest the technological promise of BCMO in future applications.

## Introduction

Double perovskite oxides with the general formula  $\text{A}_2\text{BB}'\text{O}_6$  represent a versatile class of materials that exhibit diverse physical phenomena, including quantum magnetism, colossal magnetoresistance, and complex electronic behaviors [1-5]. Their highly symmetric crystal structures—characterized by corner-sharing octahedra around alternating B and B' cations—provide an ideal platform for tuning properties via chemical substitution at A, B, or B' sites [3, 4, 6-9]. When magnetic ions occupy the B-site, they often form a face-centered cubic (FCC) sublattice, where competing exchange interactions and geometric constraints can stabilize a wide range of ground states from simple ferromagnets to frustrated antiferromagnets. Among these compounds,  $\text{Ba}_2\text{CoMoO}_6$  (BCMO; space group  $Fm-3m$ ) stands out for its rock-salt ordering of  $\text{Co}^{2+}$  and  $\text{Mo}^{6+}$  octahedra within a  $\text{Ba}^{2+}$  framework, which fosters strong antiferromagnetic interactions on the FCC Co sublattice and appreciable spin-orbit coupling effects, akin to the isovalent  $\text{Ba}_2\text{CoWO}_6$  [10-13].

X-ray absorption spectroscopy (XAS) at the Co  $L_{2,3}$  edges has been widely employed to probe valence states, local coordination, and spin states in double perovskites, with L-edge spectra providing element-specific sensitivity to the  $\text{Co}^{2+}$  high-spin configuration and Co-O covalency [14-19]. Motivated by these advances, XAS on BCMO can directly confirm the  $\text{Co}^{2+}$  valence and local crystal field effects, and benchmark the electronic structure against  $\text{Ba}_2\text{CoWO}_6$  and other Co-based double perovskites [12, 20, 21].

However, conventional solid-state synthesis of  $\text{Ba}_2\text{CoMoO}_6$  typically yields polycrystalline samples containing impurity phases such as  $\text{BaMoO}_4$  and  $\text{CoO}$ , with the former arising particularly under air annealing due to  $\text{MoO}_3$  volatility [22]. Thus, the growth of good-quality crystals is challenging. Single crystals are essential to resolve intrinsic magnetic anisotropy, frustration effects on the FCC Co sublattice, and the  $J_{\text{eff}} = 1/2$  ground state of  $\text{Co}^{2+}$  without the complications of grain boundaries, random orientations, and impurity-rich surfaces that obscure powder measurements. Prior studies have, however, been restricted to powders, leaving the intrinsic magnetic interactions, anisotropy, and magnetic ground state of  $\text{Co}^{2+}$  in single-crystalline BCMO largely unexplored.

In this work, we overcome these limitations by growing high-purity BCMO single crystals via floating-zone and top-seeded solution methods under argon, and by combining bulk characterization techniques (x-ray diffraction, magnetometry, heat capacity, surface photovoltage spectroscopy) with soft x-ray absorption spectroscopy (XAS) at the Co-L<sub>2,3</sub> edges. Our measurements on these crystals establish the cubic  $Fm-3m$  structure with reduced  $\text{BaMoO}_4$  impurity content, reveal long-range antiferromagnetic order on the FCC Co sublattice and a spin-flop transition near 26.5 kOe, and show that the magnetic entropy ( $\Delta S \approx 0.95 R \ln 2$ ) and Co L-edge XAS multiplet structure are consistent with a spin-orbit-entangled high-spin  $\text{Co}^{2+}$  ion featuring a  $J_{\text{eff}} = 1/2$  ground state, analogous to  $\text{Ba}_2\text{CoWO}_6$ . These results position  $\text{Ba}_2\text{CoMoO}_6$  as a model system for studying Co-based FCC antiferromagnets with potential spintronic and catalytic functionalities.

## Experimental Methods

### Powder Preparation

Polycrystalline BCMO was synthesized by two routes at the CoreLab Quantum Materials (HZB). First, a conventional solid-state reaction using stoichiometric  $\text{BaCO}_3$ ,  $\text{CoO}$ , and  $\text{MoO}_3$  was performed: the mixed powders were heated at 5 °C/min to 900 °C, calcined for 12 h, reground, and then heated at 5 °C/min to 1200 °C and sintered for 24 h, yielding BCMO with  $\approx 5\%$  secondary phases (mainly  $\text{BaMoO}_4$  and  $\text{CoO}$ , as identified by Powder x-ray diffraction (PXRD)). To improve phase purity, a sol-gel route was then adopted. Stoichiometric amounts (Ba:Co:Mo = 2:1:1) of  $\text{BaCO}_3$  (99.99%),  $\text{Co}(\text{CH}_3\text{COO})_2$  (99.99%), and  $(\text{NH}_4)_2\text{MoO}_4$  (prepared in situ by reacting  $\text{MoO}_3$  with aqueous  $\text{NH}_3$ ) were dissolved in deionized water with oxalic acid as a chelating agent. The solution was heated on a hot plate in air at 250 °C to remove water and form a metal-oxalate precursor, which was then calcined in air at 2 °C/min to 500 °C for 6 h and to 800 °C for 10 h with an intermediate grinding. The resulting powder was pressed into pellets and annealed at 3 °C/min to 1200 °C for 12 h in flowing argon, producing black BCMO powder with a reduced impurity fraction of 3.74% (quantified by Rietveld refinement of PXRD). Because of the volatility of  $\text{MoO}_3$ , phase purity was found to be highly sensitive to precursor stoichiometry, annealing temperature, and heating rate; therefore, heating profiles were carefully controlled and crucibles sealed to minimize contamination and Mo loss. The sol-gel argon-annealed powder was used as a precursor for crystal growth. The residual polycrystalline boules from crystal growth were used for XAS, surface photovoltage (SPV) and thermodynamic measurements.

### Crystal Growth

Single-crystal growth was attempted using an optical floating-zone furnace (Crystal Systems Corp., FZ-T-10000-H-VI-VPO) with four 300 W tungsten-halide lamps. Initial growths in air at ambient pressure showed that BCMO melts incongruently, decomposing into multiple

immiscible phases (e.g., Ba<sub>2</sub>MoO<sub>5</sub>, CoMoO<sub>4</sub>, as identified by PXRD), and did not yield stable single crystals. Subsequent trials under 2 bar Argon overpressure suppressed decomposition but still produced predominantly polycrystalline boules. Systematic improvements in the purity of the feed rods—via 2–3 cycles of annealing at 5 °C/min to 1200–1250 °C under argon for 24 h per cycle, each followed by slow cooling over 20 h—reduced impurity levels below ≈3.74% and enhanced floating-zone stability, and small single crystals (≈ 4 × 3 × 1 mm<sup>3</sup>) could be cut from the as-grown rods. These results show that both argon overpressure and high-purity starting material are crucial to mitigate incongruent melting and preserve BCMO stoichiometry.

To further stabilize single-crystal growth, additional experiments were carried out using a Czochralski furnace (Mini Czochralski Oxypuller 05-03, Cyberstar) equipped with radio frequency (RF) heating and an in-situ weighing system on the pulling rod. Growth was attempted under flowing argon at 0.5 bar overpressure with nominal pulling rates of 0.5–1.0 mm/h and crystal and melt rotation rates of 10–20 rpm. Under these conditions, the charge exhibited partially molten regions and persistent solid chunks, preventing the establishment of a stable melt zone for seeded growth. Nevertheless, slow cooling from the melt reproducibly yielded small single crystals (≈ 3 × 2.7 × 0.2 mm<sup>3</sup>) with low impurity content. Laue backscattering patterns from these crystals exhibited sharp, well-defined spots consistent with the cubic symmetry of BCMO, confirming their single-crystalline nature.

## Characterization

The structural parameters and phase purity of the polycrystalline and single-crystalline BCMO samples were examined at room temperature by powder x-ray diffraction (PXRD) using a Bruker D8 diffractometer with Cu K $\alpha$  radiation. The residual polycrystalline boules from crystal growth were used for measurements as it is closer to the crystalline material obtained in single crystals. The PXRD data were analyzed by Rietveld refinement using the *FullProf* suite to extract lattice parameters, atomic positions, and phase fractions, by refining the main phase in the cubic *Fm-3m* space group (No. 225) [23]. Magnetic properties were measured using a SQUID magnetometer in the temperature range 2–300 K and in applied magnetic fields up to 70 kOe (1 kOe = 0.1 T). Heat capacity was measured in a Physical Property Measurement System (PPMS, Quantum Design) between 2 and 300 K. Soft x-ray absorption spectroscopy (XAS) at the Co edges was carried out at the National Synchrotron Radiation Research Center (NSRRC), Hsinchu, Taiwan. The XAS measurements were performed in soft x-ray mode on the TPS45 beamline to determine the local Co electronic and magnetic state. The optical response was probed by surface photovoltage (SPV) spectroscopy at room temperature using the fixed-capacitor method with a mechanical chopper at 8 Hz for both single crystals and powders, over a photon energy range of 0.5–5 eV. XAS and SPV measurements were performed on residual polycrystalline boules obtained from crystal growth. The use of boules provides sufficient sample volume and surface area required for these spectroscopic techniques, while maintaining chemical consistency with the grown single crystals.

## Cluster-model calculations

Susceptibility and XAS spectra were simulated using the Quancy code [24–27] for a CoO<sub>6</sub><sup>10-</sup> cluster in O<sub>h</sub> symmetry. The Hamiltonian includes crystal-field (10Dq<sup>ion</sup> = 0.45 eV), spin-orbit (0.066 eV), Coulomb (U<sub>dd</sub> = 6.5 eV), charge-transfer ( $\Delta$  = 6.5 eV), and hybridization terms (V<sub>eg</sub> = 1.59 eV). Full parameter set and Wannier-LDA details as in Ref. [27] (U<sub>dd</sub> = 6.5 eV, U<sub>pd</sub> = 8.2 eV,  $\Delta$  = 6.5 eV, SOC = 0.066 eV, 10Dq(ion) = 0.45 eV, V(e<sub>g</sub>) = 1.59 eV, V(t<sub>2g</sub>) = 0.67 eV, ligand crystal field = 0.8 eV, Slater integrals reduced to 70% of Hartree–Fock values).

Magnetization computed via thermal averaging over all multiplet states; effective exchange field  $H_{\text{ex}}$  was added for intersite effects.

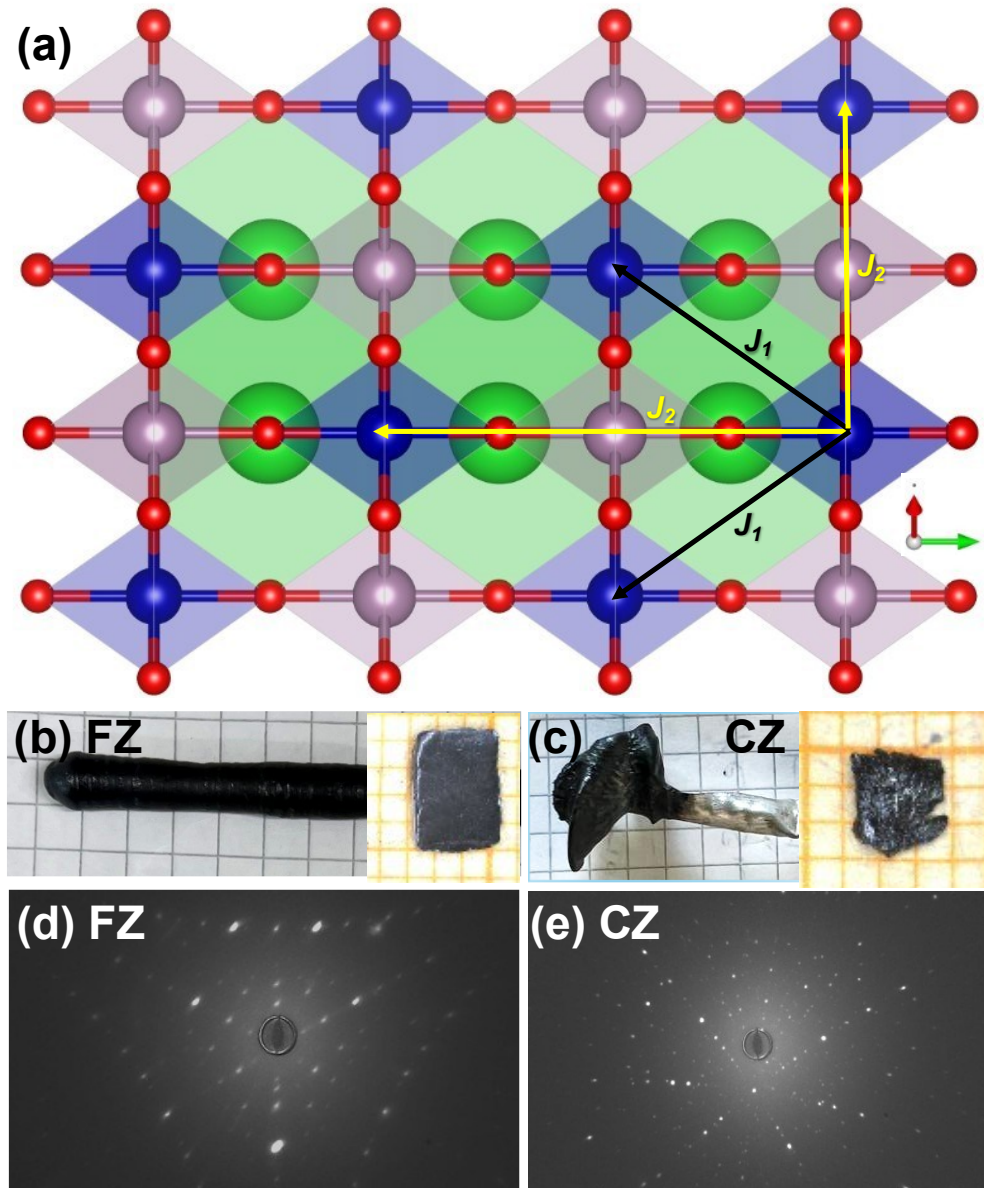


Figure 1. The Crystal structure of Ba<sub>2</sub>CoMoO<sub>6</sub> (BCMO) consists of Co<sup>2+</sup> (blue), O<sup>2-</sup> (red), Ba (green) and Mo (Magenta) ions. The arrows represent the possible magnetic exchange interactions between Co<sup>2+</sup> ions: nearest neighbor interaction ( $J_1$ , black) and next nearest neighbor interaction ( $J_2$ , yellow) through superexchange between Co-O-Mo-O-Co. (b,c) The BCMO crystals, grown using: (b) the FZ technique, and (c) the CZ technique. The insets to the right show the separated single crystals of dimensions 4\*3\*1 mm<sup>3</sup> by FZ and 3\*2.7\*0.2 mm<sup>3</sup> by CZ. (d, e) Laue diffraction patterns of these crystals from FZ and CZ growths, showing <111> and <100> symmetry, respectively.

## Results

### Structural characterization

PXRD analysis confirmed that BCMO crystallizes in a face-centered cubic structure with space group  $Fm-3m$  (225) and regular rock-salt order consisting of regular  $BaO_{12}$  cuboctahedra and regular corner-sharing  $CoO_6$  and  $MoO_6$  octahedra.  $Ba^{2+}$  occupies the  $8c$  Wyckoff position, while  $Co^{2+}$  occupies the  $4b$  position,  $Mo^{6+}$  occupies the  $4a$  position and  $O^{2-}$  occupies the  $24e$  position. All these atomic positions are fixed by the space group symmetry except for oxygen. The occupancy of Ba, Co and Mo does not change significantly from ideal stoichiometry if allowed to vary, consistent with absence of antisite disorder. The occupancy of oxygen represents a stoichiometric phase within the sensitivity limits of PXRD.

Figure 2 shows the refinement of the PXRD patterns of different samples of BCMO. The refinement factors are summarized for both powder and the CZ crystal of BCMO in Table 1. Both polycrystalline samples, prepared by solid-state synthesis and the sol-gel method, were annealed in argon and contained a significant amount of impurities ( $\approx 3.74\%$ ). The structural refinement suggested that the main impurity phase is  $BaMoO_4$  with space group  $I41/a$  (88). Nevertheless, the argon-annealed powder has a slightly smaller amount of impurities than the reported powder (4.5%)[22], which was prepared in oxygen. Both crystals grown by the CZ and FZ methods have almost the same amount of impurity (2.33(2) %).

Table 1 Rietveld Refinement parameters for BCMO samples, including the lattice parameter ( $a$ ), the  $R$  factors including the profile  $R$ -factor ( $R_p$ ), weighted-profile  $R$ -factor ( $R_{wp}$ ), and expected  $R$ -factor ( $R_{exp}$ ), the atomic positions of oxygen in the  $x$  direction ( $x(O)$ ) and the occupancy of oxygen ( $O_{occ}$ )

	Impurities (%) <b>BaMoO<sub>4</sub></b>	$a$ (Å)	$R_p$ (%)	$R_{wp}$ (%)	$R_{exp}$ (%)	$\chi^2$	$x(O)$	$O_{occ}$
<b>Polycrystal</b>	3.74(3)	8.088	3.99	5.93	2.65	5.01	0.26	1
<b>Crystal-CZ</b>	2.31(2)	8.088	5.16	7.81	2.81	7.70	0.25	1
<b>Crystal-FZ</b>	2.35(2)	8.088	4.25	8.60	3.75	8.00	0.25	1
<b>Reported [22]</b>	4.5	8.086	4.26	5.76	3.69	2.43	0.25	1

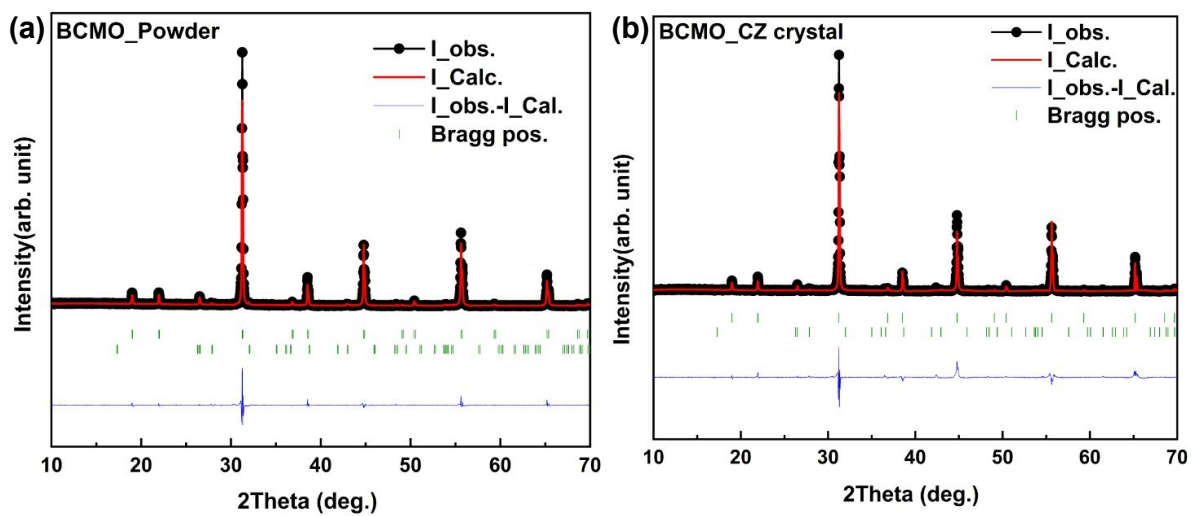


Figure 2 Rietveld refinement of the X-ray powder diffraction of BCMO: (a) Sol-gel powder with 3.74%  $BaMoO_4$ , (b) CZ crystal with 2.31%  $BaMoO_4$ . The data is represented by the black circles, while the refinement is given by the red line which included both the BCMO

(Green-Top ticks) and BaMoO<sub>4</sub>(Green-bottom ticks) phases. The blue line gives the difference between fit and data.

## Magnetic Properties

Figure 3 shows the temperature dependence of the magnetic susceptibility  $\chi(T)$  and its inverse  $1/\chi(T)$  for the polycrystalline sample and for single crystals oriented along  $\langle 100 \rangle$  and  $\langle 111 \rangle$ , measured at 0.3, 1, and 10 kOe. The polycrystalline powder exhibits a pronounced concave curvature in  $1/\chi(T)$  and contains a higher BaMoO<sub>4</sub> impurity fraction than the single crystals, as confirmed by powder X-ray diffraction. Due to the difficulty in obtaining large, high-quality single crystals of BCMO, orientation-resolved measurements were performed on separate crystals grown by different methods: a  $\langle 111 \rangle$ -oriented crystal from floating-zone (FZ) growth in argon and a  $\langle 100 \rangle$ -oriented crystal from Czochralski (CZ) growth in argon. These different growth conditions lead to small but systematic differences in crystal quality and magnetic response, with the  $\langle 100 \rangle$  crystal exhibiting an additional high-temperature feature around 300 K at high fields, consistent with residual impurities below the PXRD detection limit. For the remainder of the quantitative analysis, we therefore focus on the  $\langle 111 \rangle$  FZ crystal, which shows the cleanest intrinsic behavior as revealed by sharp Laue patterns, the absence of a large diamagnetic offset, and the lowest impurity content. All samples, regardless of morphology or growth method, exhibit the same Néel temperature of  $T_N = 20.1(1)$  K. The inverse susceptibility of all samples deviates strongly from linear Curie–Weiss behavior between about 30 and 150 K, closely resembling the response reported for BCWO and demonstrating that a simple Curie–Weiss law is not adequate [28–30]. This nonlinearity is naturally understood in terms of thermal population of low-lying excited states within the Co<sup>2+</sup> <sup>4</sup>T<sub>1</sub> multiplet in an octahedral crystal field with substantial spin–orbit coupling, rather than being attributable solely to magnetic interactions or extrinsic defects.

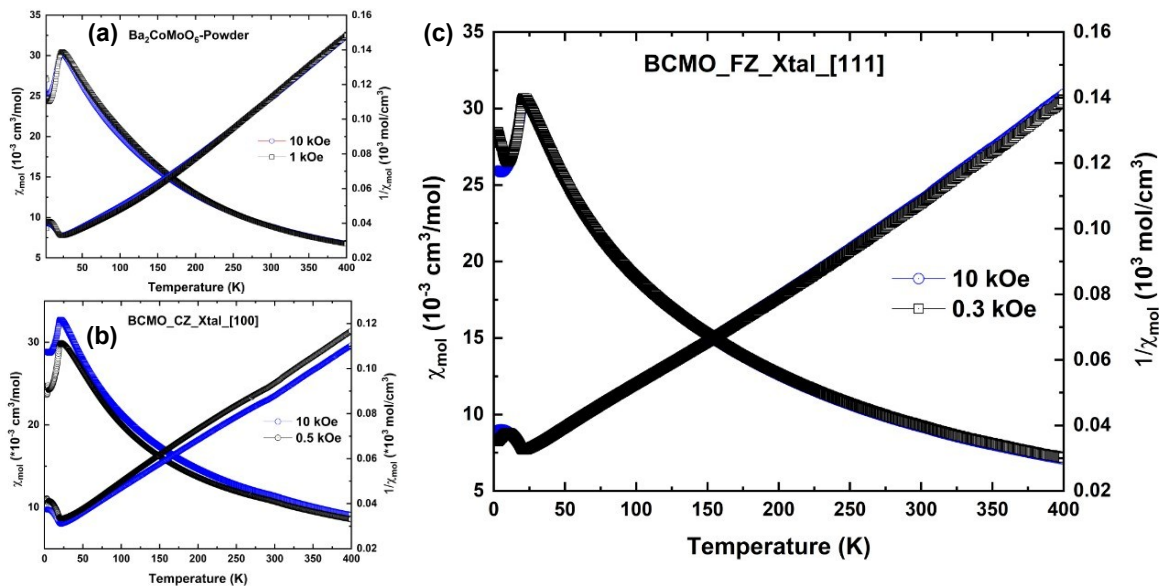


Figure 3 Temperature dependence of magnetic susceptibility (left y-axis) and inverse susceptibility (right y-axis) of BCMO samples at 0.3 and 10 kOe: (a) polycrystalline powder, (b) CZ crystal with field applied along the  $\langle 100 \rangle$  direction, and (c) FZ crystal with field along the  $\langle 111 \rangle$  direction.

To describe the Co<sup>2+</sup> response quantitatively, the susceptibility of the  $\langle 111 \rangle$  crystal at 300 Oe as well as 10000 Oe was modeled using a cluster-model Hamiltonian derived from the XAS

analysis, using the same crystal-field, spin-orbit coupling, Coulomb interaction, and hybridization parameters as in the XAS calculation, but including the external magnetic field. To account phenomenologically for intersite magnetic interactions, an effective exchange field  $H_{ex}$  was added, representing the mean-field contribution of neighbouring spins ( $H_{ex} = J_{ex} S$ , with  $J_{ex}$  fitted). The susceptibility  $\chi(T)$  was computed from the field-dependent magnetization  $M(T, B)$  of the cluster model. Excellent agreement with experiment (Figure 4) is obtained for both applied fields (0.3 kOe:  $J_{ex} \approx -0.0009$  meV; 10 kOe:  $J_{ex} \approx -0.033$  meV). The field dependence of  $J_{ex}$  reflects the phenomenological nature of the mean-field approximation:  $J_{ex}$  is an effective parameter adjusted separately for each applied field to reproduce the measured susceptibility curve above  $T_N$  and should not be interpreted as a field-dependent microscopic exchange constant. For comparison with previous reports, additional Curie–Weiss and Lloret analyses of the  $\langle 111 \rangle$  susceptibility is provided in the Supplementary Information; these parameterizations are used only to extract effective comparison parameters and are not employed in the quantitative microscopic analysis.

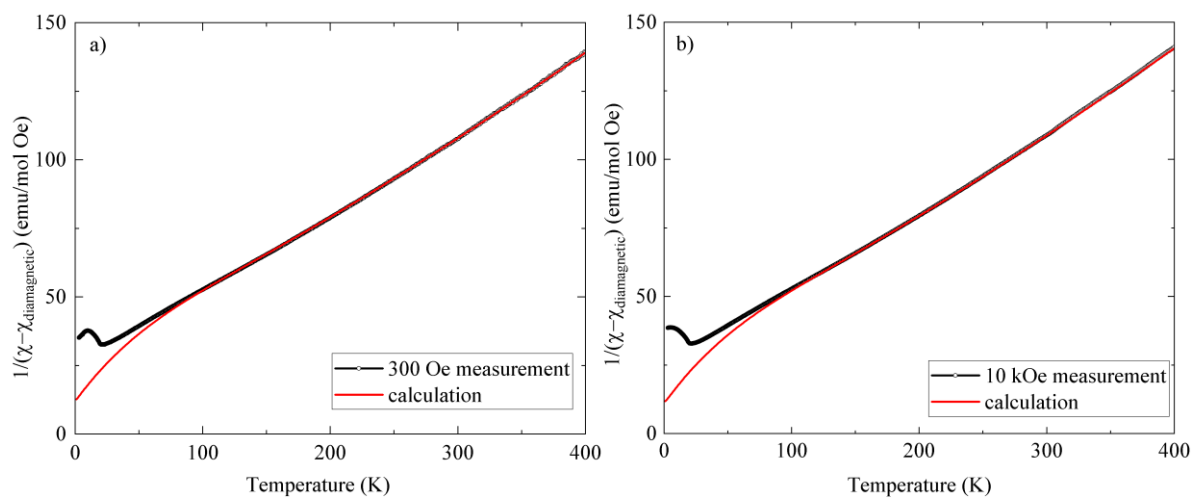


Figure 4 Temperature dependence of inverse magnetic susceptibility of BCMO samples at 0.3 (a) and 10 kOe (b) compared with simulation based on cluster model derived from XAS measurements.

The difference between the two applied field cases can be understood as follows. Under a larger magnetic field, the Co ions experience stronger effective antiferromagnetic interactions with neighboring Co ions, leading to a larger induced  $H_{ex}$ . Consequently, the 10 kOe field (which is approximately 33 times larger than 0.3 kOe) requires a  $H_{ex}$  value that is also about 33 times greater than that used for the 0.3 kOe curve. A constant offset is added to both simulated curves, since antiferromagnetic ordering can be described as causing effectively a rigid shift in the temperature dependence of the inverse susceptibility. As a result, our fitting procedure does not aim to predict the magnetic ordering temperature or to describe the behavior near and below the ordering transition. Nevertheless, it successfully reproduces the temperature dependence of the inverse susceptibility above the transition. This agreement suggests that the crystal-field energy levels extracted from XAS are consistent with those inferred from this macroscopic measurement and that the deviations observed from ideal Curie–Weiss behavior stem from crystal field excitations. A modified Curie–Weiss fit and an analytical fit following *Lloret et al.* [31] for the  $\langle 111 \rangle$  crystal are given in the Supplementary Information. The modified Curie–Weiss analysis over 200–300 K yields an apparent  $\theta_{CW}$  in the range  $-67$  to  $-72$  K, whereas the Co-specific Lloret analysis gives an effective  $\theta_{CW} = -27.4$  K together with a spin-orbit coupling  $\lambda = -185$   $\text{cm}^{-1}$ . Because susceptibility is strongly affected by low-lying spin-orbit and crystal-field excitations, these values are used only as effective reference values for comparison

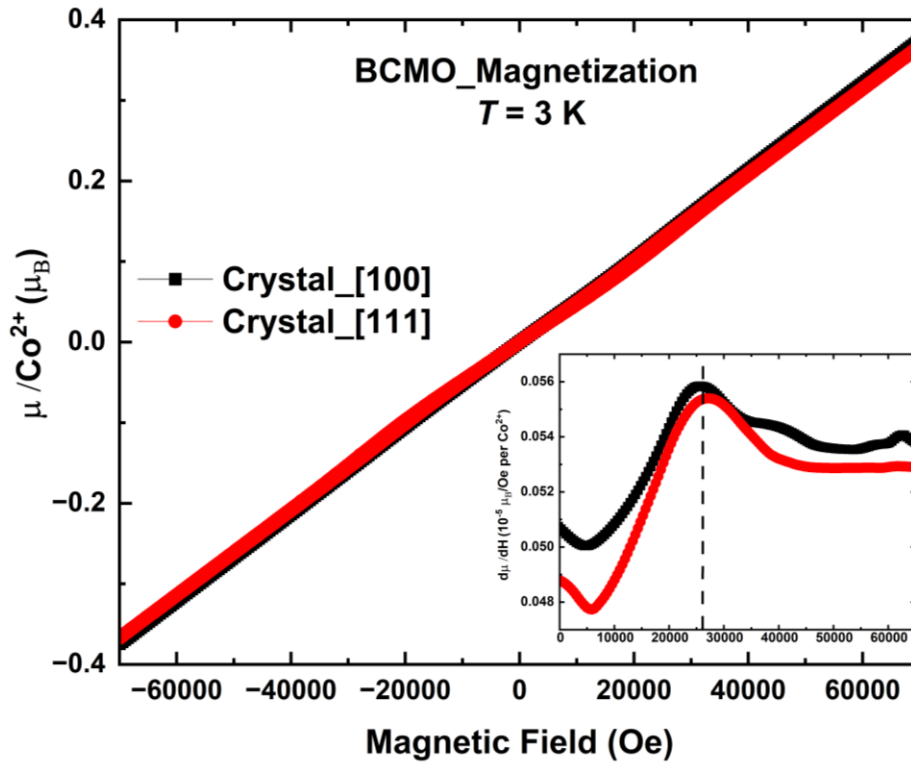


Figure 5 Isothermal magnetization of different BCMO crystals with field applied along the  $\langle 100 \rangle$  and  $\langle 111 \rangle$  directions at  $T = 3$  K. The inset shows the derivative of the effective moment per  $\text{Co}^{2+}$  ion for the directions  $\langle 100 \rangle$  (black) and  $\langle 111 \rangle$  (red). The dashed line represents a spin-flop transition around 26.5 kOe for both the  $\langle 100 \rangle$  and  $\langle 111 \rangle$  directions.

with related Co-based double perovskites, while the quantitative microscopic interpretation of the susceptibility is based on the cluster-model analysis described above.

Isothermal magnetization measurements provide evidence for the slight anisotropy of BCMO, as seen from non-linear  $M(H)$  responses and their field derivatives for crystals oriented along  $\langle 100 \rangle$  and  $\langle 111 \rangle$ . Figure 5 represents the magnetization curves and the first derivative of magnetization for the two crystalline samples at  $T = 3$  K. The measurement revealed that the magnetization of BCMO has nonlinear behavior for the  $\langle 100 \rangle$  and  $\langle 111 \rangle$  crystals. The first derivative of magnetization of  $\langle 100 \rangle$  and  $\langle 111 \rangle$  shows a pronounced peak at 26.5 kOe consistent with a spin-flop transition. Because the transition is observed for both  $\langle 100 \rangle$  and  $\langle 111 \rangle$ , the ordered moments must possess components along these directions, consistent with the behavior reported for  $\text{Ba}_2\text{CoWO}_6$  under analogous conditions [32]. The observation of a spin-flop transition implies a finite magnetic anisotropy, which stabilizes an antiferromagnetic ground state with a preferred spin orientation [33]. The spin-flop field reflects the balance between this anisotropy energy and the exchange interactions. Taken together, these results indicate that  $\text{Ba}_2\text{CoMoO}_6$  is governed by competing exchange interactions and anisotropy, leading to reduced ordering temperature relative to the overall interaction scale and the emergence of field-induced spin reorientation.

## Heat Capacity

Figure 6(a) shows the heat capacity of BCMO single crystals up to 50 K and of the polycrystalline boules up to 200 K, revealing a sharp second-order anomaly at  $T_N = 20$  K consistent with the onset of long-range antiferromagnetic order inferred from susceptibility data. No significant change was noticed in the heat capacity under different applied magnetic fields up to 90 kOe and the Néel temperature is almost field independent for all samples. The

transition peak is noticeably sharper in the crystals than in powder, reflecting higher sample quality and reduced disorder broadening in the single crystals. To isolate the magnetic contribution, the lattice heat capacity of the polycrystalline sample was modelled between 50-170 K, well above the magnetic ordering temperature  $T_N$ , using a Debye–Einstein scheme with one Debye and one Einstein branch in a 4:6 weight ratio, according to the equation:

$$c_p(T) = 3Rn \left( 0.4 \left( \frac{T}{\theta_D} \right)^3 \int_0^{\frac{\theta_D}{T}} \frac{x^4 e^x}{(e^x - 1)^2} dx + 0.6 \left( \frac{\theta_E}{T} \right)^2 \frac{e^{\theta_E/T}}{(e^{\theta_E/T} - 1)^2} \right),$$

where  $R$  is the universal gas constant,  $n$  is the number of ions per formula unit which is  $n = 10$  for BCMO, and  $\theta_D, \theta_E$  are the Debye and Einstein temperatures, respectively. The resulting fit yields  $\theta_D = 284(3)$  K and  $\theta_E = 598(4)$  K which provide an excellent description of the phonon background over the chosen window and a stable baseline for extracting the magnetic heat capacity,  $c_{\text{mag}}$ , by extrapolating to low temperature and subtracting from the measured data. The extracted magnetic heat capacity and entropy changes are shown in Figure 6(b).

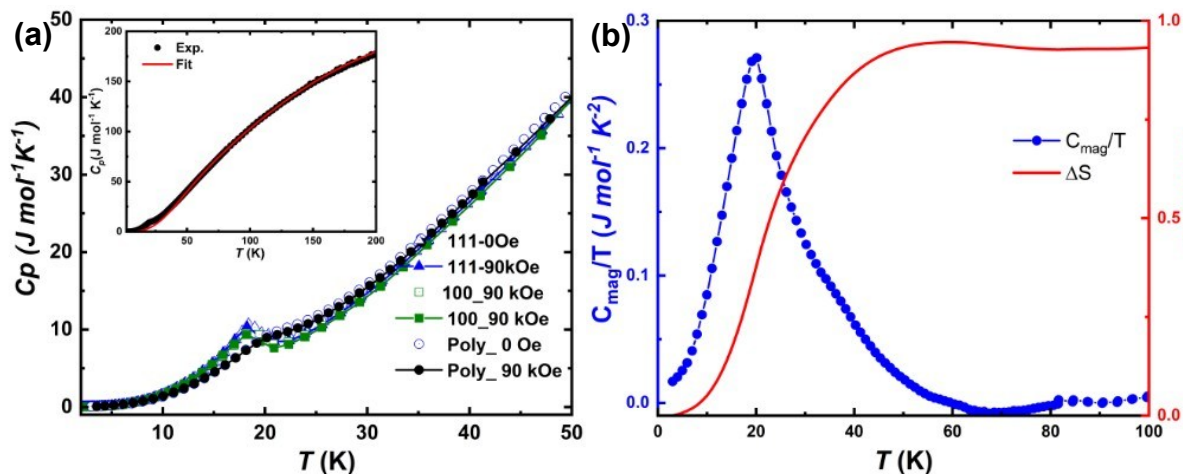


Figure 6 (a) Heat capacity of BCMO crystals for magnetic field applied along the  $\langle 100 \rangle$  and  $\langle 111 \rangle$  directions and for the sol-gel polycrystals. The inset shows the modelling of the heat capacity of BCMO polycrystalline sample at zero field using Debye and Einstein models to subtract the magnetic contribution of the heat capacity in the temperature range 50-150 K. (b) Magnetic contribution of the heat capacity over temperature for the polycrystalline sample at zero field. The change in entropy is shown on the left axis in units of  $R \ln 2$ .

The entropy change  $\Delta S$  was calculated by integrating  $c_{\text{mag}}/T$  in the range 2-50 K. The magnetic entropy saturates at  $\sim 50$  K at the value  $5.5(1) \text{ J mol}^{-1} \text{ K}^{-1}$  or  $0.95(2) R \ln 2$ . The ground state is  $J_{\text{eff}} = 1/2$  similar to  $\text{Ba}_2\text{CoWO}_6$  [32]. The saturation value of  $0.95(2) R \ln 2$  is consistent within uncertainty with a doublet ground state described by  $J_{\text{eff}} = 1/2$ , for which  $\Delta S = R \ln(2J + 1) = R \ln 2$ . About 50% of the entropy is released above the Néel temperature up to 50 K, suggesting strong short-range magnetic correlations in this temperature range, which is a characteristic feature of frustrated systems. This extended release of entropy above  $T_N$ , together with the effective Curie-Weiss temperature obtained from the supplementary Lloret analysis,  $\theta_{\text{CW}} \approx -27.4$  K, the frustration index  $f = \theta_{\text{CW}}/T_N \approx 1.36$ , places BCMO in the weakly frustrated regime. We emphasize that this frustration index is based on an effective susceptibility parameterization given in Supplementary Information, while the microscopic interpretation of the susceptibility in the main text is based on the XAS-derived cluster-model analysis. The slightly lower value of entropy change could be attributed to a conservative

phonon-background subtraction together with minor secondary phases, resulting in slightly underestimating the extracted entropy.

## Electronic structure

To probe the electronic and magnetic properties of BCMO we performed temperature dependent X-ray absorption spectroscopy (XAS) using the inverse partial fluorescence yield method [34, 35], which is suitable for extremely insulating samples, in a similar manner to what is reported in [36]. For this experiment the sol-gel polycrystalline sample was used. XAS is extremely sensitive to the local electronic structure, and when combined with theoretical modelling to simulate the measured spectra, it is possible to obtain information about the ground state quantum numbers and effective crystal field parameters [26, 28, 37-40]. XAS experiments were performed at beamline TPS45 of the National Synchrotron Radiation Research Center in Taiwan [41]. A polycrystalline sample was mounted in an aluminum sample holder and cleaved in ultra-high vacuum conditions before being transferred in-vacuo to the measurement chamber with a base pressure of  $\sim 10^{-11}$  mbar.

Figure 7 shows the temperature-dependent isotropic Co  $L_{2,3}$  XAS spectra of BCMO. In XAS the measured spectra are separated into the two  $L_2$  and  $L_3$  edges due to  $2p$  spin orbit coupling. The obtained line shape is characteristic of a  $\text{Co}^{2+}$  valence, which we further verify with our calculations. The present temperature dependence originates from the thermal population of low-lying excited states with increasing temperature. This behavior is expected for high-spin  $\text{Co}^{2+}$  ions in octahedral coordination [28].

To obtain further information about the electronic structure of the compound, we performed full-multiplet configuration-interaction cluster calculations for a  $\text{CoO}_6$  cluster using  $O_h$  point group. Hybridization parameters were obtained from wannierized LDA band structure [42]. The DFT calculations were performed with FPLO [43] and the cluster-interaction calculations with the Quanty code [24-27]. The full set of parameters used in our calculations can be found in [27]. Our calculations include  $3d$ - $3d$  and  $2p$ - $3d$  Coulomb interactions, spin-orbit coupling for both  $2p$  and  $3d$  shell, hybridization with oxygen ligands and crystal-field effects. We obtain a very good agreement between experiment and calculation, implying that our model accurately captures most details of the local electronic structure of  $\text{Co}^{2+}$  ions in this material.

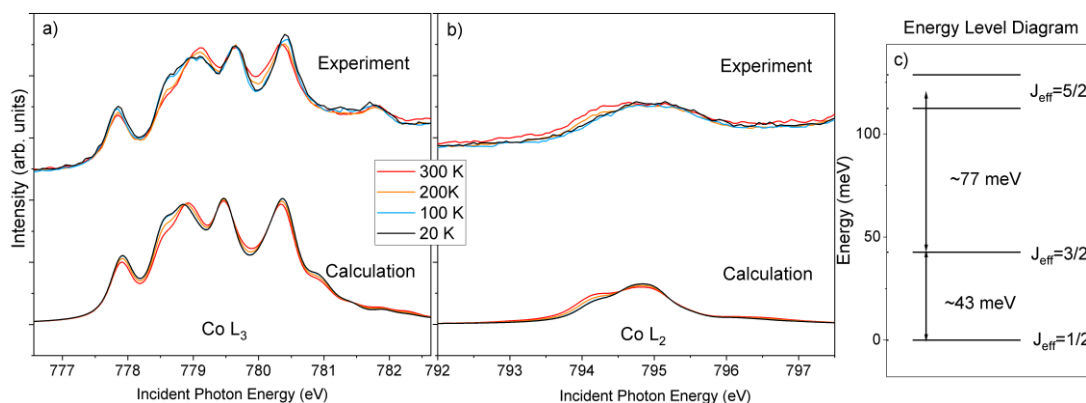


Figure 7 Experimental and calculated temperature dependence of measured and theoretical XAS spectra of  $\text{Ba}_2\text{CoMoO}_6$  for the (a)  $L_3$  and (b)  $L_2$  Co edges and (c) the corresponding energy level diagram.

From our model we can estimate an effective crystal field splitting of 0.6 eV. We find the first low lying spin-orbit coupling excited state at 43 meV, as shown in Figure 7 (c). We estimate the  $g$  factor using the relation  $\Delta E = g\mu_B B$ , where  $\Delta E$  is the splitting of the doublet due to magnetic field in a calculation with applied field of 6 T at 0 K, we obtain a value of  $g = 4.52$ .

Surface photovoltage (SPV) spectroscopy is a surface-sensitive probe of electronic structure that reports on near-surface band bending, photocarrier separation, and optically driven excitations, thereby providing indirect yet informative constraints on crystal-field and charge-transfer processes [31, 44-46].

For BCMO, theoretical studies predict Co-derived electronic structures with spin-polarized states and possible half-metallic character, but comprehensive experimental optical datasets remain scarce; SPV thus offers complementary spectroscopic insight alongside the limited UV–visible data available for related double perovskites [31, 44-46]. The SPV spectra of BCMO, Figure 8, exhibits a strong optical response, with an onset above 1.25 eV, a pronounced peak at 2.65 eV, and a subsequent decrease in intensity, up to 4.5 eV. The SPV signal exhibits an onset at approximately 1.5 eV, indicating the energy scale at which photo-induced charge separation becomes significant. We note that SPV is sensitive to surface and near-surface electronic processes, and therefore this onset should be interpreted as an effective photoresponse threshold rather than a direct measurement of the bulk bandgap. The additional features observed in the spectra suggest the presence of multiple photoactive transitions, which may arise from a combination of intrinsic electronic structure and surface-related effects[31, 44-46]. Combining SPV with ellipsometry or diffuse-reflectance spectroscopy and targeted first-principles calculations would further refine the level scheme and disentangle *d-d*, charge-transfer, and band-to-band contributions. Overall, the robust SPV response with a prominent 2.65 eV feature underscores the potential of BCMO for spintronic optoelectronics and energy-conversion applications where strong photo response and tunable spectral sensitivity are desirable. Further measurements using bulk-sensitive optical probes would be required to determine the intrinsic bandgap.

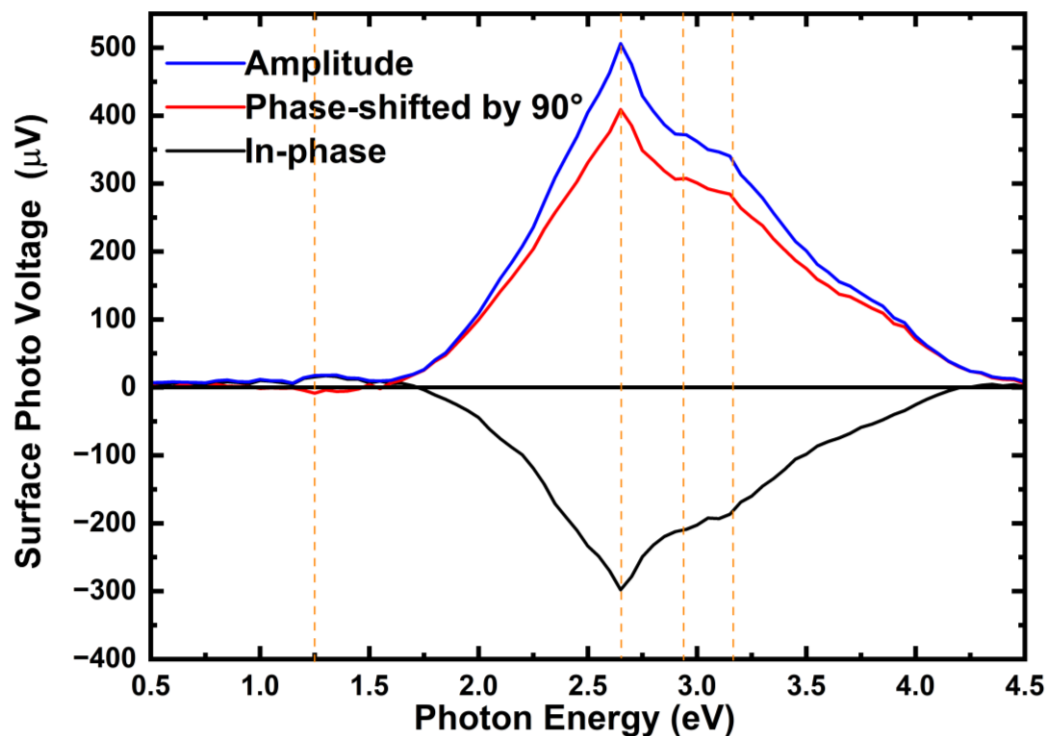


Figure 8 (a) Surface photovoltage (SPV) measurement of polycrystalline pellets of BCMO plotted as a function of photon energy: The in-phase signal (X component) (black), the phase-

shifted by 90° signal (Y component) (red), and the SPV amplitude (composed of both X and Y components) (blue). The dashed orange lines represent the absorption of the BCMO phase.

## Conclusions

This work establishes high-quality Ba<sub>2</sub>CoMoO<sub>6</sub> (BCMO) single crystals as a robust platform for studying intrinsic magnetic and electronic properties of face-centered cubic (FCC) antiferromagnets with strong spin–orbit coupling. Optimized floating-zone and top-seeded solution growth under argon atmosphere produced crystals with reduced BaMoO<sub>4</sub> impurity fractions compared to the powder samples, confirming the cubic *Fm-3m* structure with lattice parameter  $a = 8.088 \text{ \AA}$ . Sharp X-ray diffraction peaks, well-defined Laue patterns, and consistent magnetic transitions across all samples validate the improved crystal quality.

Magnetic susceptibility and heat capacity measurements consistently reveal long-range antiferromagnetic ordering at  $T_N = 20.1(1) \text{ K}$ , which is unaffected by applied fields up to 90 kOe. Quantitative analysis of the  $\langle 111 \rangle$  single-crystal susceptibility using the cluster model derived from XAS analysis reproduces the measured curve, showing that deviations from Curie Weiss are due to spin-orbit and crystal field excitations. The Debye–Einstein analysis of the specific heat reveals recovery of magnetic entropy of  $0.95 R \ln 2$ , suggesting a Kramers doublet consistent with the ground state determined by spin-orbit splitting. Isothermal magnetization reveals a spin-flop transition at 26.5 kOe for both the  $\langle 100 \rangle$  and  $\langle 111 \rangle$  orientations, indicating weak magneto-crystalline anisotropy and ordered-moment components along these crystallographic directions. X-ray absorption spectroscopy independently verifies the Co<sup>2+</sup> valence state, the local octahedral crystal-field scheme, the doubly degenerate ground state with  $J_{eff} = 1/2$  character and yielding  $g = 4.52$ , consistent with the enhanced moment observed in susceptibility. Surface photovoltage spectroscopy suggests a strong optical response linked to crystal-field and band-structure transitions, implying potential for optoelectronic applications, though bulk optical measurements (ellipsometry, diffuse reflectance) would complement this surface-sensitive SPV data.

Collectively, these results position Ba<sub>2</sub>CoMoO<sub>6</sub> alongside Ba<sub>2</sub>CoWO<sub>6</sub> as a model weakly frustrated FCC antiferromagnet, distinguished by its robust  $J_{eff} = 1/2$  ground state, modest anisotropy, and accessible spin-flop behavior. The weak-frustration assignment is supported by the effective Curie-Weiss scale extracted from the supplementary susceptibility analysis, while the microscopic description of the magnetic response is provided by the XAS-derived cluster model. Future work combining single-crystal neutron diffraction, bulk optical spectroscopy, and first-principles calculations will refine the magnetic structure, clarify electronic-level assignments, and assess opportunities for spintronic and energy-conversion applications suggested by the spin-flop transition and strong photovoltage response, as a clear, field-controlled way to reorient the Néel vector and strongly change transport signals.

## Conflict of interest

The authors declare no conflict of interest.

## Acknowledgements

We acknowledge the CoreLab Quantum Materials at Helmholtz Zentrum Berlin für Materialien und Energie (HZB), Germany, where the powder and single crystal samples of Ba<sub>2</sub>CoMoO<sub>6</sub> were synthesized and characterized. The authors acknowledge the support of Igal Levine and Thomas Dittrich from the Solar Energy Division, HZB, for performing the surface photovoltage measurements. M.M.F.-C. greatly acknowledges funding from the Deutsche Forschungsgemeinschaft (DFG, German Research Foundation) Grant No. 387555779. Work

at MPI-CPfS Dresden and HZB was partially supported by SFB1143 (Project No. 247310070). The authors acknowledge the support from the Max Planck-POSTECH-Hsinchu Center for Complex Phase Materials.

## References

1. D.C. Binwal, P.P. Mudoi, D.P. Panda, P. Vishnoi, Molybdenum chloride double perovskites: dimensionality control of optical and magnetic properties, *Chemical Science*, 14 (2023) 3982-3989.
2. L.A. Muscarella, E.M. Hutter, Halide Double-Perovskite Semiconductors beyond Photovoltaics, *ACS Energy Letters*, 7 (2022) 2128-2135.
3. S. Liu, Y. Cheng, S. Yan, J. He, L. Deng, H. Luo, Unravelling the Electromagnetic Behavior in Ordered Double-Perovskite  $\text{Sr}_2\text{FeMoO}_6$ , *Journal of Electronic Materials*, 51 (2022) 3430-3437.
4. H. Mutch, O. Mustonen, H.C. Walker, P.J. Baker, G.B.G. Stenning, F.C. Coomer, E.J. Cussen, Long- and short-range magnetism in the frustrated double perovskite  $\text{Ba}_2\text{MnWO}_6$ , *Physical Review Materials*, 4 (2020) 014408.
5. K.I. Kobayashi, T. Kimura, H. Sawada, K. Terakura, Y. Tokura, Room-temperature magnetoresistance in an oxide material with an ordered double-perovskite structure, *Nature*, 395 (1998) 677-680.
6. Rachedi, R. Baghdad, A. Nacef, Magnetic, optoelectronic and thermodynamic properties of the double perovskite  $\text{Ba}_2\text{NiWO}_6$  in its stable antiferromagnetic phase, *Optik*, 227 (2021) 166032.
7. H.L. Feng, Z. Deng, C.U. Segre, M. Croft, S.H. Lapidus, C.E. Frank, Y. Shi, C. Jin, D. Walker, M. Greenblatt, High-Pressure Synthesis of Double Perovskite  $\text{Ba}_2\text{NiIrO}_6$ : In Search of a Ferromagnetic Insulator, *Inorganic Chemistry*, 60 (2021) 1241-1247.
8. M. Vogl, R. Morrow, A.A. Aczel, R.B. Rodriguez, A.U.B. Wolter, S. Wurmehl, S. Aswartham, B. Büchner, Complex magnetic properties in the mixed 4f-5d double perovskite iridates  $\text{X}_2\text{ZnIrO}_6$  ( $\text{X} = \text{Nd, Sm, Eu, Gd}$ ), *Physical Review Materials*, 4 (2020) 054413.
9. H.L. Feng, S. Calder, M.P. Ghimire, Y.-H. Yuan, Y. Shirako, Y. Tsujimoto, Y. Matsushita, Z. Hu, C.-Y. Kuo, L.H. Tjeng, T.-W. Pi, Y.-L. Soo, J. He, M. Tanaka, Y. Katsuya, M. Richter, K. Yamaura,  $\text{Ba}_2\text{NiOsO}_6$ : A Dirac-Mott insulator with ferromagnetism near 100 K, *Physical Review B*, 94 (2016) 235158.
10. Q. Yao, S.-Y. Lv, Z. Yu, Y.-C. Chang, C.-W. Pao, Z. Hu, L.-M. Yang, X. Huang, Q. Shao, J. Lu, Face-Centered Cubic Ruthenium Nanocrystals with Promising Thermal Stability and Electrocatalytic Performance, *ACS Catalysis*, 13 (2023) 11023-11032.
11. R.L. Zhang, L. Damewood, Y.J. Zeng, H.Z. Xing, C.Y. Fong, L.H. Yang, R.W. Peng, C. Felser, Two prospective Li-based half-Heusler alloys for spintronic applications based on structural stability and spin-orbit effect, *Journal of Applied Physics*, 122 (2017).
12. T. Hiram, N. Tsujii, H. Kitazawa, G. Kido, La-substitution effects on double perovskite compound  $\text{Ba}_2\text{CoMoO}_6$ , *Physica B: Condensed Matter*, 359-361 (2005) 1336-1338.

13. T. Li, W. Guo, Q. Shi, Development and performance of A-site rich perovskite-type material for enhanced oxygen evolution reaction in alkaline electrolyte, *Journal of Materials Science: Materials in Electronics*, 31 (2020) 21272-21278.
14. Y.Y. Chin, Z. Hu, H.J. Lin, S. Agrestini, J. Weinen, C. Martin, S. Hébert, A. Maignan, A. Tanaka, J.C. Cezar, N.B. Brookes, Y.F. Liao, K.D. Tsuei, C.T. Chen, D.I. Khomskii, L.H. Tjeng, Spin-orbit coupling and crystal-field distortions for a low-spin  $3d^5$  state in  $BaCoO_3$ , *Physical Review B*, 100 (2019) 205139.
15. H.J. Lin, Y.Y. Chin, Z. Hu, G.J. Shu, F.C. Chou, H. Ohta, K. Yoshimura, S. Hébert, A. Maignan, A. Tanaka, L.H. Tjeng, C.T. Chen, Local orbital occupation and energy levels of Co in  $Na_xCoO_2$ : A soft x-ray absorption study, *Physical Review B*, 81 (2010) 115138.
16. T. Burnus, Z. Hu, H.H. Hsieh, V.L.J. Joly, P.A. Joy, M.W. Haverkort, H. Wu, A. Tanaka, H.J. Lin, C.T. Chen, L.H. Tjeng, Local electronic structure and magnetic properties of  $LaMn_{0.5}Co_{0.5}O_3$  studied by x-ray absorption and magnetic circular dichroism spectroscopy, *Physical Review B*, 77 (2008) 125124.
17. T. Burnus, Z. Hu, M.W. Haverkort, J.C. Cezar, D. Flahaut, V. Hardy, A. Maignan, N.B. Brookes, A. Tanaka, H.H. Hsieh, H.J. Lin, C.T. Chen, L.H. Tjeng, Valence, spin, and orbital state of Co ions in one-dimensional  $Ca_3Co_2O_6$ : An x-ray absorption and magnetic circular dichroism study, *Physical Review B*, 74 (2006) 245111.
18. Y.-Y. Chin, Z. Hu, Y. Shimakawa, J. Yang, Y. Long, A. Tanaka, L.H. Tjeng, H.-J. Lin, C.-T. Chen, Charge and spin degrees of freedom in A-site ordered  $YCu_3Co_4O_{12}$  and  $CaCu_3Co_4O_{12}$ , *Physical Review B*, 103 (2021) 115149.
19. Q. Che, M. Ghiasi, L. Braglia, M.L.J. Peerlings, S. Mauri, P. Torelli, P. de Jongh, F.M.F. de Groot, Operando Soft X-ray Absorption of  $LaMn_{1-x}Co_xO_3$  Perovskites for CO Oxidation, *ACS Catalysis*, 14 (2024) 11243-11251.
20. D. Jha, A. Himanshu, B. Singh, D. Shukla, U. Kumar, R. Kumar, K. Bhattacharyya, A. Sindhe, P. Krishna, A. Dutta, T. Sinha, R. Ray, The X-ray photoelectron and Co K-edge absorption spectra of  $Ba_2CoWO_6$ , 2019.
21. X. Wang, J. Zhang, Z. Pan, D. Lu, M. Pi, X. Ye, C. Dong, J. Chen, K. Chen, F. Radu, S. Francoual, S. Agrestini, Z. Hu, C.-F. Chang, A. Tanaka, K. Yamaura, Y. Shen, Y. Long, X-ray Absorption Spectroscopic Study of the Transition-Metal-Only Double Perovskite Oxide  $Mn_2CoReO_6$ , *The Journal of Physical Chemistry C*, 128 (2024) 15668-15675.
22. María J. Martínez-Lope, José A. Alonso, María T. Casais, María T. Fernández-Díaz, Preparation, Crystal and Magnetic Structure of the Double Perovskites  $Ba_2CoBO_6$  (B = Mo, W), *European Journal of Inorganic Chemistry*, 2002 (2002) 2463-2469.
23. J. Rodríguez-Carvajal, Recent advances in magnetic structure determination by neutron powder diffraction, *Physica B: Condensed Matter*, 192 (1993) 55-69.
24. Y. Lu, M. Hoepfner, O. Gunnarsson, M.W. Haverkort, Efficient real-frequency solver for dynamical mean-field theory, *Physical Review B*, 90 (2014) 085102.
25. M.W. Haverkort, G. Sangiovanni, P. Hansmann, A. Toschi, Y. Lu, S. Macke, Bands, resonances, edge singularities and excitons in core level spectroscopy investigated within the dynamical mean-field theory, *Europhysics Letters*, 108 (2014) 57004.
26. H.J. Lin, Local orbital occupation and energy levels of Co in  $Na_xCoO_2$ : A soft X-ray absorption study, *Physical Review B*, 81 (2010) 115138.

27. Parameter set:  $U_{dd} = 6.5$  eV,  $U_{pd} = 8.2$  eV, charge transfer energy  $\Delta = 6.5$  eV, SOC = 0.066 eV, ionic crystal field  $10Dq(\text{ion}) = 0.45$  eV, hybridization  $V(\text{eg}) = 1.59$  eV,  $V(\text{t}_{2g}) = 0.67$  eV, ligand crystal field = 0.8 eV. Slater integrals reduced to 70% of Hartree-Fock values.
28. T. Burnus, Local electronic structure and magnetic properties of  $\text{LaMn}_{0.5}\text{Co}_{0.5}\text{O}_3$  studied by X-ray absorption and magnetic circular dichroism spectroscopy, *Physical Review B*, 77 (2008) 125124.
29. S. Mugiraneza, A.M. Hallas, Tutorial: a beginner's guide to interpreting magnetic susceptibility data with the Curie-Weiss law, *Communications Physics*, 5 (2022) 95.
30. K.Y. Povarov, J. Wosnitza, A.R.N. Hanna, A.T.M.N. Islam, B. Lake, S.A. Zvyagin, Electron Spin Resonance in the Double-Perovskite Oxide Antiferromagnet  $\text{Ba}_2\text{CoWO}_6$ , *Applied Magnetic Resonance*, 56 (2025) 1549-1558.
31. F. Lloret, M. Julve, J. Cano, R. Ruiz-García, E. Pardo, Magnetic properties of six-coordinated high-spin cobalt(II) complexes: Theoretical background and its application, *Inorganica Chimica Acta*, 361 (2008) 3432-3445.
32. A.R.N. Hanna, A. Islam, C. Ritter, S. Luther, R. Feyerherm, B. Lake, Growth of  $\text{Ba}_2\text{CoWO}_6$  single crystals and their magnetic, thermodynamic and electronic properties, *J Phys Condens Matter*, 36 (2024).
33. A.N. Bogdanov, A.V. Zhuravlev, U.K. Rößler, Spin-flop transition in uniaxial antiferromagnets: Magnetic phases, reorientation effects, and multidomain states, *Physical Review B*, 75 (2007) 094425.
34. A.J. Achkar, Determination of total X-ray absorption coefficient using non-resonant X-ray emission, *Scientific Reports*, 1 (2011) 182.
35. A.J. Achkar, Bulk sensitive X-ray absorption spectroscopy free of self-absorption effects, *Physical Review B*, 83 (2011) 081106.
36. M.M. Ferreira-Carvalho, Trigonal distortion in the Kitaev candidate honeycomb magnet  $\text{BaCo}_2(\text{AsO}_4)_2$ , *Physical Review B*, 112 (2025) 125135.
37. F.M.F. De Groot, X-ray absorption and dichroism of transition metals and their compounds, *Journal of Electron Spectroscopy and Related Phenomena*, 67 (1994) 529-622.
38. Y.Y. Chin, Spin-orbit coupling and crystal-field distortions for a low-spin  $3d^5$  state in  $\text{BaCoO}_3$ , *Physical Review B*, 100 (2019) 205139.
39. T. Burnus, Valence, spin, and orbital state of Co ions in one-dimensional  $\text{Ca}_3\text{Co}_2\text{O}_6$ : An X-ray absorption and magnetic circular dichroism study, *Physical Review B*, 74 (2006) 245111.
40. Tanaka, T. Jo, Resonant 3d, 3p, and 3s photoemission in transition metal oxides predicted at 2p threshold, *Journal of the Physical Society of Japan*, 63 (1994) 2788.
41. H.M. Tsai, A submicron soft X-ray active grating monochromator beamline for ultra-high-resolution angle-resolved photoemission spectroscopy, *AIP Conference Proceedings*, 2054 (2019) 060047.
42. M.W. Haverkort, M. Zwierzycki, O.K. Andersen, Multiplet ligand-field theory using Wannier orbitals, *Physical Review B*, 85 (2012) 165113.

43. K. Koepnik, H. Eschrig, Full-potential nonorthogonal local-orbital minimum-basis band-structure scheme, *Physical Review B*, 59 (1999) 1743.
44. C. Toro, A. Rebaza, J. Villa, D.A. Téllez, J. Roa-Rojas, Half-metallic electronic feature and thermophysical properties of the  $\text{Ba}_2\text{CoMoO}_6$  perovskite-like cobalt molybdate, *Revista UIS Ingenierías*, 19 (2020) 213-223.
45. Suzuki, T. Oku, Effects of transition metals incorporated into perovskite crystals on the electronic structures and magnetic properties by first-principles calculation, *Heliyon*, 4 (2018) e00755.
46. M. Nabi, S.S. Padelkar, J.J. Jasieniak, A.N. Simonov, A. Alam, Lead-free magnetic double perovskites for photovoltaic and photocatalysis applications, *Physical Review Applied*, 21 (2024) 014063.

## Supplementary Information

### Magnetic and Electronic Properties of Ba<sub>2</sub>CoMoO<sub>6</sub> Single Crystals

A.R.N. Hanna<sup>1,\*</sup>, M. M. Ferreira-Carvalho<sup>2,3</sup>, S.H. Chen<sup>2</sup>, C. F. Chang<sup>2</sup>, C. Y. Kuo<sup>4,5</sup>,  
A.T.M.N. Islam<sup>1</sup>, R. Feyerherm<sup>1</sup>, L.H. Tjeng<sup>2</sup>, B. Lake<sup>1,6,\*</sup>

<sup>1</sup>Helmholtz-Zentrum Berlin für Materialien und Energie GmbH, 14109 Berlin, Germany

<sup>2</sup>Max Planck Institute for Chemical Physics of Solids, Nöthnitzer Str. 40, 01187 Dresden

<sup>3</sup>Germany and Institute of Physics II, University of Cologne, Zùlpicher Straße 77, 50937 Cologne, Germany

<sup>4</sup>Department of Electrophysics, National Yang Ming Chiao Tung University, Hsinchu, Taiwan

<sup>5</sup>National Synchrotron Radiation Research Center, Hsinchu, Taiwan

<sup>6</sup>Institut für Festkörperphysik, Technische Universität Berlin, Germany

\*Corresponding authors : [Abanoub.Hanna@helmholtz-berlin.de](mailto:Abanoub.Hanna@helmholtz-berlin.de), [Bella.lake@helmholtz-berlin.de](mailto:Bella.lake@helmholtz-berlin.de)

## Magnetic Properties

### 1. Curie-Weiss Model

For quantitative analysis of the Curie–Weiss behaviour, we focused on the <111> crystal because it exhibits the cleanest high-temperature regime and the least extrinsic contributions, as evidenced by the absence of a large diamagnetic offset and by Laue patterns indicative of high crystalline quality. By contrast, the powder sample displays a pronounced concave curvature in  $1/\chi(T)$ , and the <100> crystal shows a high-temperature feature around 300 K and an enhanced susceptibility, both consistent with residual impurity contributions below the PXRD detection threshold and therefore unsuitable for extracting intrinsic Co<sup>2+</sup> parameters with high confidence. These observations are consistent with the phase analysis, which shows reduced BaMoO<sub>4</sub> fractions in the single crystal relative to the powders, and motivate restricting Curie–Weiss fitting and moment estimates to the <111> data set for reliable determination of  $\mu_{\text{eff}}$ ,  $g$ , and  $\theta_{\text{CW}}$  [1].

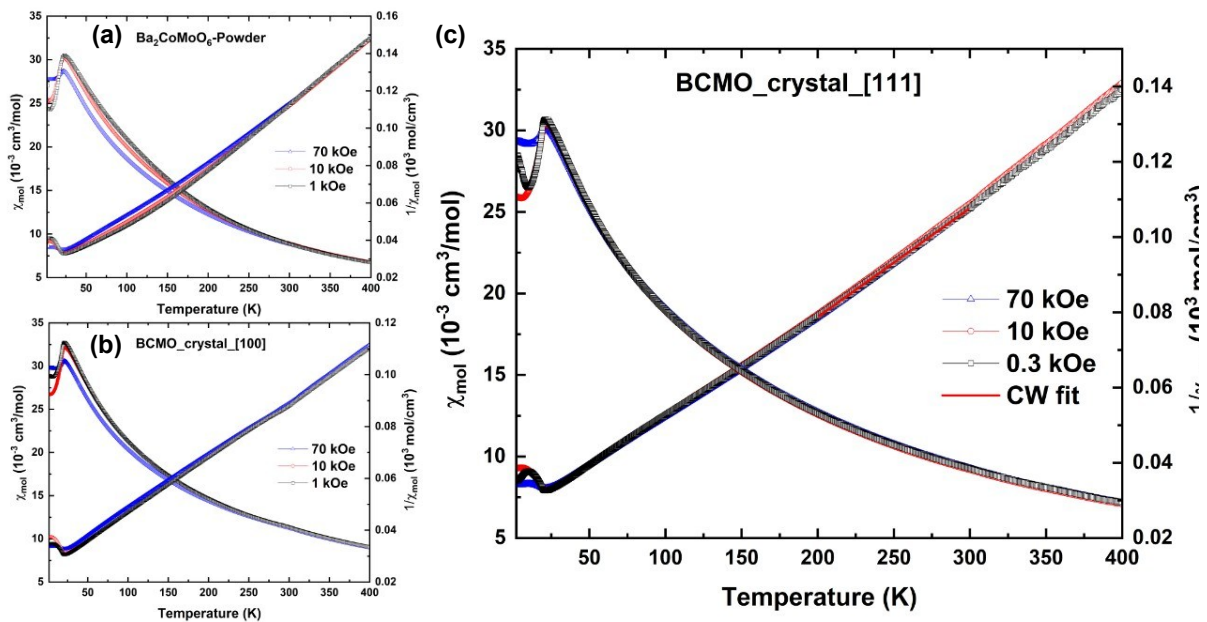


Figure SI-1: Temperature dependence of magnetic susceptibility (left y-axis) and inverse susceptibility (right y-axis) of BCMO samples at 1, 10, 70 kOe: (a) polycrystalline powder, (b) crystal along <100> direction, and (c) crystal along <111> direction

For comparison with previous reports, the inverse susceptibility of the  $\langle 111 \rangle$  crystal was fitted in the temperature range 200–300 K with a modified Curie–Weiss model including a temperature-independent diamagnetic correction  $\chi_0 = -1.44 \times 10^{-4} \text{ cm}^3/\text{mol}$ , obtained from tabulated core diamagnetism values for the constituent ions[2]. The corresponding Curie–Weiss fit yields an apparent Curie–Weiss temperature  $\theta_{CW}$  in the range  $-67$  to  $-72$  K and an effective moment  $\mu_{eff} \approx 5.2(1) \mu_B$ , in agreement with previous reports on related Co-based double perovskites. These Curie–Weiss parameters are used only as reference values for comparison with  $\text{Ba}_2\text{CoWO}_6$  (BCWO) and are not employed for detailed quantitative analysis[1].

The Curie–Weiss analysis of the  $\langle 111 \rangle$  single crystal in the temperature range 200–300 K yields an effective magnetic moment  $\mu_{eff}=5.2(1) \mu_B$  and a large effective  $g = 6.0(1)$ , which exceed the spin-only value for high-spin  $\text{Co}^{2+}$  with  $S=3/2$  and indicate a substantial orbital contribution arising from spin–orbit coupling in the octahedral crystal field of BCWO. These values are consistent with the formation of a Kramers doublet and an effective  $j_{eff}= 1/2$  ground state, as also inferred from the entropy release approaching  $R \ln 2$  and by analogy to the isovalent double perovskite  $\text{Ba}_2\text{CoWO}_6$ , where similar  $g$  factors and  $\mu_{eff}$  were reported[3]. The negative Curie–Weiss temperature  $\theta_{CW} = -67$  to  $-72$  (1) K confirms dominant antiferromagnetic exchange on the FCC Co sublattice. In addition, the nonlinearity of the inverse susceptibility between approximately 30 and 150 K mirrors the behavior in  $\text{Ba}_2\text{CoWO}_6$  and is naturally explained by thermal population of low-lying excited states of the  $\text{Co}^{2+}$  multiplet manifold in the octahedral crystal field.

Table 1 Fitting values for the inverse susceptibility of BCWO  $\langle 111 \rangle$  crystal according to the Curie–Weiss model. Where  $H$  is the applied magnetic field,  $\theta_{CW}$  is the Curie–Weiss temperature and  $\mu_{eff}$  is the effective moment.

<b>Ba<sub>2</sub>CoMoO<sub>6</sub></b> <b>200-300 K</b> <b><math>\langle 111 \rangle</math></b>	<b>H = 1 kOe</b>		<b>H = 10 kOe</b>		<b>H = 70 kOe</b>	
	<b><math>\theta_{CW}(\text{K})</math></b>	<b><math>\mu_{eff}(\mu_B)</math></b>	<b><math>\theta_{CW}(\text{K})</math></b>	<b><math>\mu_{eff}(\mu_B)</math></b>	<b><math>\theta_{CW}(\text{K})</math></b>	<b><math>\mu_{eff}(\mu_B)</math></b>
	-72(1)	5.3(1)	-69(1)	5.2(1)	-67(1)	5.2(1)

## 2. Lloret model

To describe the  $\text{Co}^{2+}$  response quantitatively within an analytical framework, the susceptibility of the  $\langle 111 \rangle$  crystal at 300 Oe was also analysed using the model developed for six-fold coordinated high-spin  $\text{Co}^{2+}$  complexes by *Lloret et al.* [4]. In this approach, the temperature and spin-orbit dependence of the effective moment  $\mu_{eff}(T, \lambda)$  is encoded in closed-form expressions obtained for the  $^4T_1(\text{F})$  ground term in an octahedral crystal field. The susceptibility data were fitted to the equation:

$$\chi_{mol} = \chi_0 + \frac{N_A \mu_0 \mu_B^2}{3k_B(T - \theta_{CW})} \mu_{eff}^2$$

with

$$\mu_{eff}^2(T, \lambda) = 3 \frac{c_1 + c_2 \frac{k_B T}{\lambda} + (c_3 + c_4 \frac{k_B T}{\lambda}) \exp\left(\frac{9\lambda}{4k_B T}\right) + (c_5 + c_6 \frac{k_B T}{\lambda}) \exp\left(\frac{6\lambda}{k_B T}\right)}{1 + 2 \exp\left(\frac{9\lambda}{4k_B T}\right) + 3 \exp\left(\frac{6\lambda}{k_B T}\right)}$$

Here,  $\chi_0$  is the temperature-independent contribution,  $\theta_{CW}$  is the effective Curie-Weiss temperature,  $\lambda$  is the spin-orbit coupling parameter, and the coefficients  $c_1$ – $c_6$  are fixed numerical constants tabulated by Lloret et al. [21]. In this model, the effective moment approaches  $\mu_{eff} = 3.75 \mu_B$  for  $T \rightarrow 0$  and increases with  $T$  up to  $\mu_{eff} = 5.3 \mu_B$  at 300 K, consistent with the high-temperature Curie-Weiss analysis.

For the  $\langle 111 \rangle$  crystal, this Co-specific model yields an average spin-orbit coupling  $\lambda \approx -185 \text{ cm}^{-1}$ , corresponding to a level splitting between the ground state doublet and the first excited quartet of  $9|\lambda|/4 \approx 416 \text{ cm}^{-1}$ , i.e.  $\approx 51.6 \text{ meV}$ . The effective  $\theta_{CW} \approx -27.4 \text{ K}$  is substantially smaller in magnitude than the apparent  $\theta_{CW}$  obtained from the simple Curie-Weiss analysis over 200–300 K. The negative sign of this effective  $\theta_{CW}$  confirms dominant antiferromagnetic interactions on the Co sublattice. We emphasise that the Lloret model provides a phenomenological parameterisation specific to high-spin  $\text{Co}^{2+}$  complexes and is used here to extract effective comparison parameters, while the main microscopic description of the susceptibility is based on the XAS-derived cluster model discussed in the main text. This effective value of  $\theta_{CW} \approx -27.4 \text{ K}$  is the physically appropriate scale for computing the frustration index, because the simple Curie-Weiss analysis over 200–300 K overestimates the interaction scale by including contributions from spin-orbit excited states of the  $\text{Co}^{2+}$  multiplet.

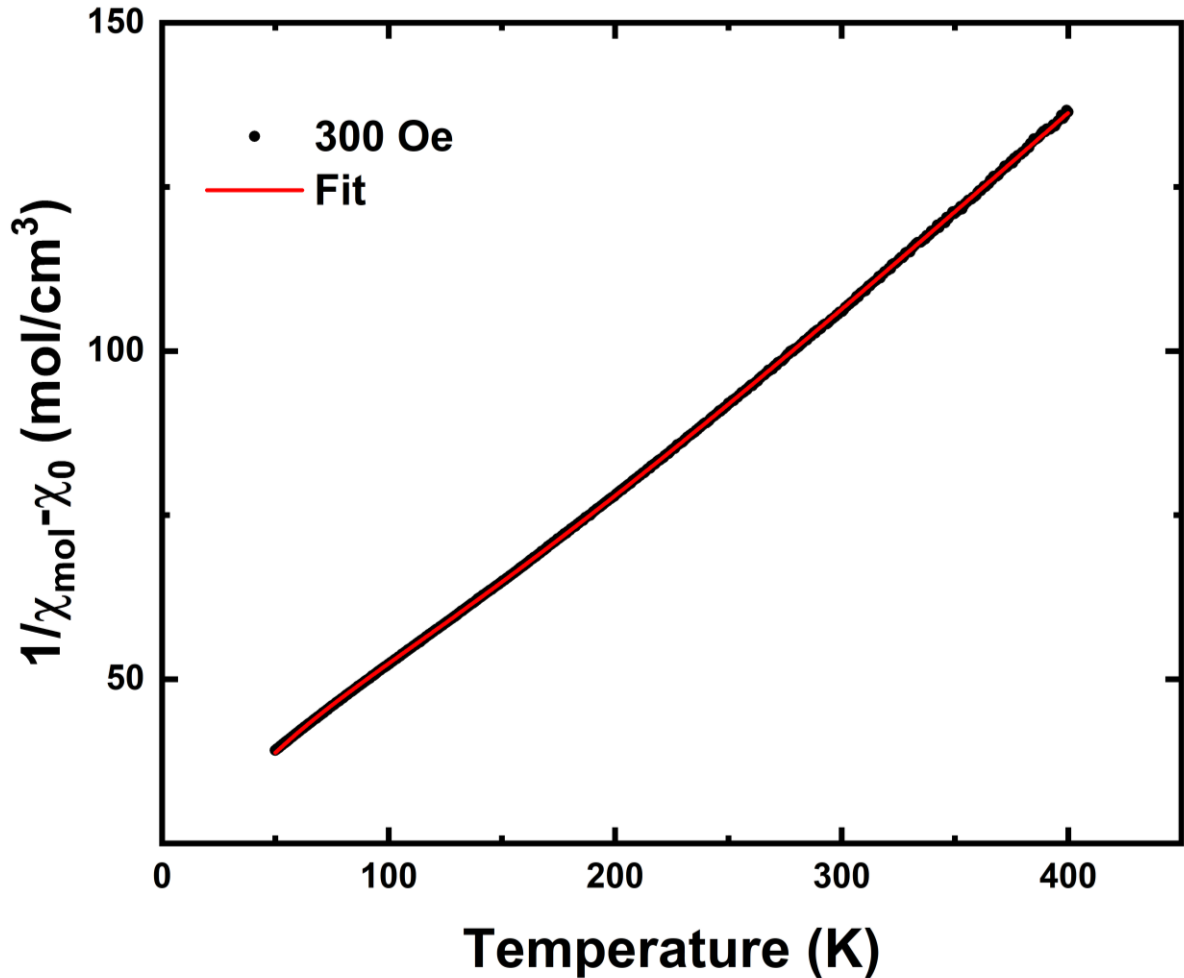


Figure SI-2 : Temperature dependence of magnetic susceptibility (left y-axis) and inverse susceptibility (right y-axis) of BCMO FZ crystal at 0.3 kOe with field along the  $\langle 111 \rangle$  direction.

## References

1. Hanna, A.R.N., et al., *Growth of Ba<sub>2</sub>CoWO<sub>6</sub> single crystals and their magnetic, thermodynamic and electronic properties*. J Phys Condens Matter, 2024. **36**(50).
2. Bain, G.A. and J.F. Berry, *Diamagnetic Corrections and Pascal's Constants*. Journal of Chemical Education, 2008. **85**(4): p. 532.
3. Martínez-Lope, María J., J. Alonso, and María T. Casais, *Synthesis, Crystal and Magnetic Structure of the Double Perovskites A<sub>2</sub>NiMoO<sub>6</sub> (A = Sr, Ba): A Neutron Diffraction Study*. European Journal of Inorganic Chemistry, 2003. **2003**: p. 2839-2844.
4. Lloret, F., et al., *Magnetic properties of six-coordinated high-spin cobalt(II) complexes: Theoretical background and its application*. Inorganica Chimica Acta, 2008. **361**(12): p. 3432-3445.